Available online at www.sciencedirect.com
ScienceDirect
Physics of the Earth and Planetary Interiors 165 (2007) 176–193
PHYSICS OF THE EARTH AND PLANETARY INTERIORS
www.elsevier.com/locate/pepi

Structure of the crust beneath the southeastern Tibetan Plateau from teleseismic receiver functions

Lili Xu [*], Stéphane Rondenay, Robert D. van der Hilst

Department of Earth, Atmospheric, and Planetary Sciences, Massachusetts Institute of Technology, 77 Massachusetts Avenue, Cambridge, MA 02139, USA

Received 23 August 2006; received in revised form 10 September 2007; accepted 11 September 2007

Abstract

Southeastern Tibet marks the site of presumed clockwise rotation of the crust due to the India–Eurasian collision and abutment against the stable Sichuan basin and South China block. Knowing the structure of the crust is a key to better understanding of crustal deformation and seismicity in this region. Here, we analyze recordings of teleseismic earthquakes from 25 temporary broadband seismic stations and one permanent station using the receiver function method. We find that the crustal thickness decreases gradually from the Tibetan Plateau proper to the Sichuan basin and Yangtze platform but that significant (intra-)crustal heterogeneity exists on shorter lateral scales (<1000 km). Most receiver functions reveal a time shift of ∼0.2 s in the direct P arrival and negative phases between 0 and 5 s after the first arrival. Inversion of the receiver functions yields S-velocity profiles marked by near-surface and intra-crustal low-velocity zones (IC-LVZs). The shallow low-velocity zones are consistent with the wide distribution of thick surface sedimentary layers. The IC-LVZ varies laterally in depth and strength; it becomes thinner toward the east and southeast and is absent in the Sichuan basin and the southern part of the Yangtze platform. Results from slant-stacking analysis show a concomitant decrease in crust thickness from ∼60 km in the Songpan-Ganze fold system to ∼46 km in the Sichuan basin and ∼40 km in the Yangtze platform. High Poisson's ratios (>0.30) are detected beneath the southeastern margin of Tibet but in the Sichuan basin and southeastern Yangtze platform the values are close to the global average. Combined with high regional heat flow and independent evidence for mid-crustal layers of high (electric) conductivity, the large intra-crustal S-wave velocity reduction (12–19%) and the intermediate-to-high average crustal Poisson's ratios are consistent with partial melt in the crust beneath parts of southeastern Tibet. These results could be used in support of deformation models involving intra-crustal flow, with the caveat that significant lateral variation in location and strength of this flow may occur.
Published by Elsevier B.V.

Keywords: Southeastern Tibet; Receiver function; Moho discontinuity; S-wave velocity profile; Low-velocity zone; Partial melt

---

1. Introduction

Geological structures suggest that deformation in the central part of the Tibetan Plateau, directly north of the Indian subcontinent, has largely been the result of north–south convergence (Molnar and Tapponnier, 1975; Rowley, 1996). However, east of the Himalayan syntaxis, the east–west trending structural features of central Tibet bend southeastward as a consequence of the extrusion of crustal elements from central Tibet, their abutment against the Sichuan basin and South China block, and the stress field caused by subduction under the Burma ranges (King et al., 1997; Chen et al., 2000; Wang et al., 2001; Lev et al., 2006). The left-lateral Xianshuihe–Xiaojiang

---

[*] Corresponding author. Tel.: +1 617 252 1974; fax: +1 617 258 0620.
E-mail address: lilixu@mit.edu (L. Xu).

0031-9201/$ – see front matter. Published by Elsevier B.V.
doi:10.1016/j.pepi.2007.09.002

fault system forms the eastern boundary of the clockwise rotation (Avouac and Tapponnier, 1993; Wang and Burchfiel, 2000).

Following Chen et al. (1987) and Wang et al. (2003) we recognize four major geological units southeast of the Tibetan Plateau proper: the Yangtze Platform, the Songpan-Ganze fold system, the Sanjiang fold system, and the Bomi-Tengchong fold system (Fig. 1). The Songpan-Ganze and Sanjiang fold belts are separated from the Yangtze Platform by the Longmen Shan fault and the Red River fault, respectively. The Sichuan basin is located to the east of the Longmen Shan fault and is part of the Yangtze platform. Surface sediments of up to 10 km thickness are widespread throughout the study region (Leloup et al., 1995; Song and Lou, 1995; Burchfiel and Wang, 2003). The Tengchong area belongs to the Bomi-Tengchong fold system, with volcanic activity in the Cenozoic.

The crustal structure in Tibet has been debated. For example, previous shear-wave splitting studies (e.g., McNamara et al., 1994; Sandvol et al., 1997) indicated that the mantle anisotropy is aligned with surface structures. These results were interpreted by Silver (1996) and Sandvol et al. (1997) to represent, at least in central Tibet, a high degree of mechanical coupling between the upper crust and the upper mantle, or, at least, that the lower crust is strong enough to transfer shear stresses between the crust and mantle over horizontal length scales of tens of kilometers. In contrast, geologic and GPS studies (Burchfiel et al., 1995; Chen et al., 2000; Wang et al., 2001) showed little to no convergence across a large part of eastern Tibet, implying that eastern Tibet has been uplifted without appreciable shortening of the upper crust, and that crustal thickening involved primarily shortening within the deep crust. Royden and co-workers explained this observation as well as the evolution in shape of river streams with a channel flow model in which the deep crust is weak and in which there is little correlation between the crustal and upper mantle deformation (Royden et al., 1997; Clark and Royden, 2000; Roy and Royden, 2000a,b; Clark et al., 2005).

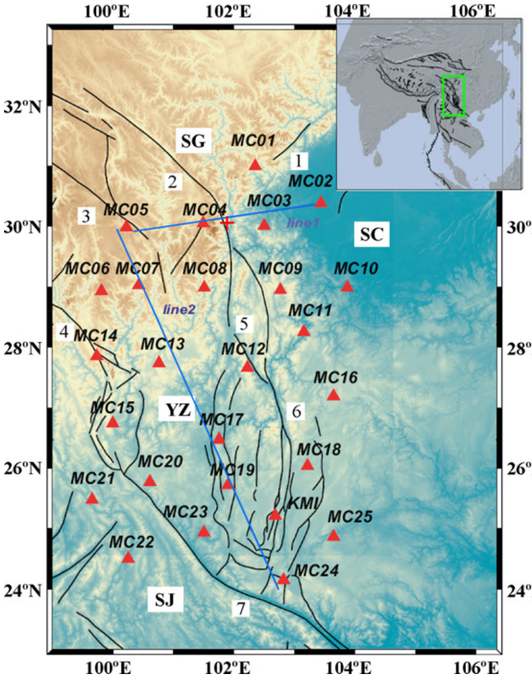

Fig. 1. Location of seismic stations (red triangles) and cross-sections (blue lines) in the study region (boxed area on the inset map). Red cross represents the Konga Shan area. The background shows the topography of southeastern Tibet and the regional faults: (1) Longmen Shan fault; (2) Xianshuihe fault; (3) Lijiang fault; (4) Zhongdian fault; (5) Anninghe fault; (6) Xiaojiang fault; (7) Ailaoshan Red-River fault. The main geological units are: SG, Songpan-Ganze fold system; YZ, Yangtze platform; SJ, Sangjiang fold zone; SC, Sichuan basin (modified from Chen et al., 1987 and Wang et al., 2003). The Bomi-Tengchong fold system is located outside of the mapped area, starting ∼80 km to the west of station MC21.

Regional shear-wave splitting measurements are consistent with some level of decoupling of crust and upper mantle beneath parts of the study region (Lev et al., 2006). The interpretation of teleseismic shear-wave splitting measurements is often ambiguous, however. Indeed, opposite conclusions have been reached from joint modeling of shear-wave splitting and GPS results, using a thin viscous sheet approach (Silver, 1996; Holt, 2000; Flesch et al., 2005).

Receiver function studies in central Tibet (Kind et al., 1996; Nelson et al., 1996; Yuan et al., 1997; Ozacar and Zandt, 2004) presented evidence for a crustal low-velocity zone. This could be, and has been, used in support of the crust-mantle decoupling and middle/lower crustal flow, but to date the observations have been too sparse to determine whether this crustal low-velocity zone extends into the southeastern part of the Tibetan Plateau. Moreover, as we will show here, it is likely that neither end-member model is correct and that significant lateral variation exists in the nature of crust-mantle coupling and – if present at all – in the depths where intra-crustal flow might occur.

To date, most estimates of crustal thickness for southeastern Tibet are derived from deep seismic sounding profiles and from the coherence between gravity anomalies and topography (e.g., Lin et al., 1993; Li and Mooney, 1998; Wang et al., 2003). Previous receiver function studies in the Yunnan province (Hu et al., 2003; He et al., 2004) suggest that a crustal low-velocity zone exists in the upper and/or lower crust of the western Yangtze platform. Furthermore, the high average crustal

Poisson's ratio of >0.30 (Hu et al., 2003) for this area suggests the existence of partial melt in the crust (Owens and Zandt, 1997). Body-wave tomography (Huang et al., 2002; Wang et al., 2003) revealed low-velocity anomalies in the crust and upper mantle of various areas (e.g., the western Sichuan Plateau and the Panxi tectonic zone). Such intra-crustal low-velocity zones (IC-LVZs) are also apparent in results of high-resolution surface wave array tomography (Yao et al., 2006, submitted). In combination, these previous studies suggest that the crust beneath southeastern Tibet is highly heterogeneous.

In order to improve the characterization of this heterogeneity we analyze data from a regional network of 25 temporary broadband seismometers (Fig. 1). We use receiver function analysis, which has been used previously to characterize the crust (including IC-LVZs) in a variety of tectonic environments (e.g., Langston, 1979; Gurrola et al., 1995; Owens and Zandt, 1997; Yuan et al., 1997; Bostock, 1998; Zorin et al., 2002). We first use a simultaneous deconvolution approach to obtain the average crustal impulse response (Gurrola et al., 1995; Bostock, 1998). Then, we use a slant-stacking method to constrain simultaneously the crustal thickness (*H*) and P-to-S wave velocity ratio (V_P/V_S) (Chevrot and van der Hilst, 2000; Zhu and Kanamori, 2000). Finally, we derive S-wave velocity profiles through least-squares inversion of the receiver function waveforms and simplify the derived models into fewer layered models (Owens et al., 1984; Ammon et al., 1990; Kind et al., 1995). Such inversions have been used in previous studies to image low-velocity layers within the crust (e.g., Kind et al., 1996; Frederiksen et al., 2003; Hetland et al., 2004) and can be used to estimate both the depth to and thicknesses of the IC-LVZs.

2. Methodology

2.1. Receiver functions

The receiver function technique derives a source-equalized teleseismic waveform, in which source, far field path, and instrument effects are removed by deconvolving the vertical component from the radial/transverse components (Langston, 1979; Gurrola et al., 1995; Bostock, 1998). The resulting receiver function waveform is an estimate of the ground's impulse response. For stations MC01-MC25, the gains were the same on all channels, whereas for station KMI they differed by <3% between channels. No equalization before rotation was performed for the latter due to the small difference in gain, which we believe does not strongly affect our results. In this study, the following processing steps are applied to derive the receiver functions: rotation, deconvolution, moveout correction, stacking, and filtering. First, all teleseismic traces are rotated from an *E–N–Z* coordinate system to an *R–T–Z* system (Fig. 2). Second, we deconvolve the vertical components from both the radial and transverse components to remove the effects of the source and the instrument. During this process, which is conducted in the frequency domain, we apply a water level to stabilize the spectral division (e.g., Langston, 1979; Bostock, 1998). The water level is adjusted to the quality of the original seismogram and the stability of the equalization; it varies from 10^{-3} to10^{-1}.

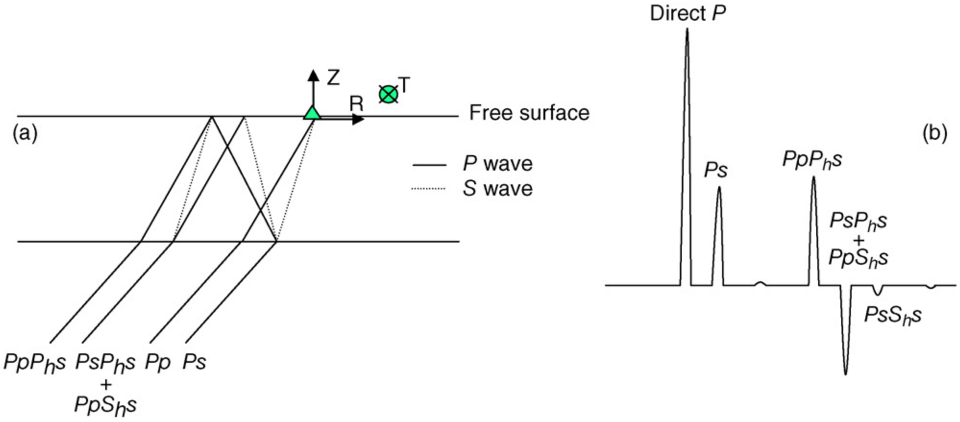

Fig. 2. A schematic representation of receiver functions: (a) simplified ray diagram showing the main P-to-S converted phases for a layer over a half-space, and (b) corresponding receiver function waveform. Vertical, radial, and transverse components of the wavefield are denoted *Z*, *R*, and *T*, respectively. Except for the first arrival, upper case letters denote downgoing travel paths, lower case letters denote upgoing travel paths, and *h* indicates reflection from the interface (modified from Ammon et al., 1990).

Third, a Gaussian filter with width of 2.0 Hz is applied in the frequency domain after deconvolution to remove high frequency noise in the seismogram. To improve the overall signal-to-noise ratio and ensure stability of the deconvolution process, we simultaneously deconvolve all seismograms along moveout curves, which depend on the horizontal slowness and the depth of phase conversion (Bostock, 1998); this provides an average ground impulse response of the sampling area.

The lateral offset between the surface recording point and conversion point at depth is a function of the ray parameter, the crustal thickness, and the average crustal velocity. For example, for a ray parameter of 0.0586 s/km (P-wave from a source at 67° distance), crust thickness of 40 km, and crust velocities $V_P = 6.2$ km/s and $V_S = 3.6$ km/s, the $P_m s$ phases sample the Moho ∼9 km from the stations, while multiples sample it ∼40 km away.

2.2. Slant-stacking method

Crust thickness H and average V_P/V_S of the crust can be estimated from the relative timing of P-to-S conversions and reverberations (see Fig. 2). Here, we follow the approach of Zhu and Kanamori (2000) and use the travel times of three phases relative to the direct P (see Fig. 2 for definitions): $P_h s$, $PpP_h s$, and $PpS_h s$ (or $PsP_h s$). The differential travel-time equations depend on H, V_P/V_S, the average crustal P-wave velocity, and the ray parameter (p). We determine the ray parameter from the event depth and epicentral distance and use average crustal P-wave velocities of 6.2 and 6.4 km/s (Lin et al., 1993; Li and Mooney, 1998; Wang et al., 2003). At each station, we sum the amplitudes of the receiver functions at the predicted differential travel times of the Ps, $PpPs$, and $PpSs$ (or $PsPs$) phases for a given H and V_P/V_S

$$s\left(H, \frac{V_P}{V_S}\right) = \sum_N [a(t_{P-Ps}) + a(t_{P-PpPs}) + a(t_{P-PpSs})] \tag{1}$$

where N is the number of receiver functions at each station and $a(t)$ is the amplitude of a receiver function at time t. We perform a grid search in the $V_P/V_S - H$ parameter space, and take the optimum solution to be at the maximum of the amplitude stack surface. We use the 90% contour lines as an indication of uncertainty (Hetland et al., 2004). In an isotropic medium, the Poisson's ratio (ν) is given by

$$\nu = \frac{1}{2}\left(1 - \frac{1}{(V_P/V_S)^2 - 1}\right). \tag{2}$$

The Poisson's ratio is an important parameter for determining crustal composition because it is sensitive to mineralogy (e.g., Christensen, 1996) and the presence of fractures, fluid content, and partial melt (e.g., O'Connell and Budiansky, 1974; Mavko, 1980).

2.3. Least-squares inversion and velocity modeling

A least-squares inversion of receiver function waveforms is performed to estimate the crustal velocity structure (Ammon et al., 1990). This technique is more sensitive to velocity contrasts than to the absolute magnitude of the velocities, but it requires a starting velocity model that is close to the actual velocities (Owens et al., 1984; Ammon et al., 1990). Here, we accommodate this requirement by using the seismic refraction results of Zhu et al. (personal communication, 2003) as our starting velocity models. We invert for velocity structures consisting of horizontal layers with fixed thicknesses of 2 km, not because we expect to resolve such detail, but because the receiver functions are dominated by shear-converted phases with a typical wave length of ∼8 km and layers as thin as 2 km may influence the inverse modeling. Furthermore, we fix the Poisson's ratios and Moho depths at the values derived from the slant-stacking method. We invert only for the S-wave velocity; the P-wave velocity is derived from these results in conjunction with the V_P/V_S ratio. Approximate densities (ρ) throughout the model are derived using the equation $\rho = 0.32V_P + 0.77$ (Berteussen, 1977).

The inversion seeks to minimize the difference between the observed and model-generated receiver function waveforms. A distribution of possible solutions is built by running the inversion for a range of starting models based on perturbations to the prescribed initial model (see Ammon et al., 1990), and the preferred solution is computed by averaging the solutions that fit the data within data uncertainty using a χ^2-test with 95% confidence (Lodge and Helffrich, 2006; see Appendix I in Supplementary data for details). At each station, we apply varying levels of smoothing until we can model the dominant phases and avoid over-complexity in the resultant model.

Since the inversion tends to overfit the data and produce solutions that may contain too much structure, we proceed by simplifying the preferred crustal model to obtain a model that is more realistic and, therefore, easier to interpret (see, e.g., Lodge and Helffrich, 2006). Simplified models are constructed by investigating the effects of isolated portions of the least-squares solution on the receiver function waveform. Velocity gradient are replaced by single, sharp discontinuities, and adjacent model layers exhibiting similar velocities are grouped to form a coarser model. Once the minimum structure has been identified, the solution to this “simplified model” is found by performing a grid-search over its parameters and computing the average of all the models that fit the data within 95% confidence (Lodge and Helffrich, 2006; see Appendix I in Supplementary data for details).

3. Data

We use data from a network of 25 temporary broadband seismometers operated by MIT and the Chengdu Institute of Geology and Mineral Resources (CIGMR) for 1 year between September 2003 and October 2004. The station distribution is shown in Fig. 1. We analyze waveforms from seismic events that are selected based on the following criteria: (1) body-wave magnitude $m_b > 5.6$ to insure high signal-to-noise ratio, (2) epicentral distances (Δ) between 30° and 100° to avoid wavefield complexities due to upper mantle discontinuities or diffraction at the core-mantle boundary. In order to get relatively simple source functions, earthquakes with vertical waveforms containing two or more obvious pulses are avoided. In addition, data with poor signal-to-noise ratios are discarded. This includes, for example, data with no obvious first-P arrivals and/or large-amplitude surface waves in the observing time window.

With a deployment period of 1 year only, our array recorded data from a relatively narrow range of backazimuths. A total of 147 events, mostly from the circum-Pacific seismogenic belt (Fig. 3), were used to produce 1329 individual receiver function waveforms. However, due to equipment failure, periods of high noise levels, and variable durations of station operation, only a subset of the total number of events were recorded at a particular station. In addition, we used data recorded between 1990 and 2002 at KMI (Kunming), a station of the China Digital Seismograph Network (CDSN). The number of events selected for analysis at each station is given in Table 1.

4. Results

4.1. Receiver functions from 25 temporary stations

At most stations, P-to-S conversions from the Moho are clearly identified on both individual and stacked receiver functions. Other prominent phases are observed after the direct P arrival, indicating the presence of significant intra-crustal structure. We illustrate our analysis with data from stations MC22 and MC05 (Fig. 4).

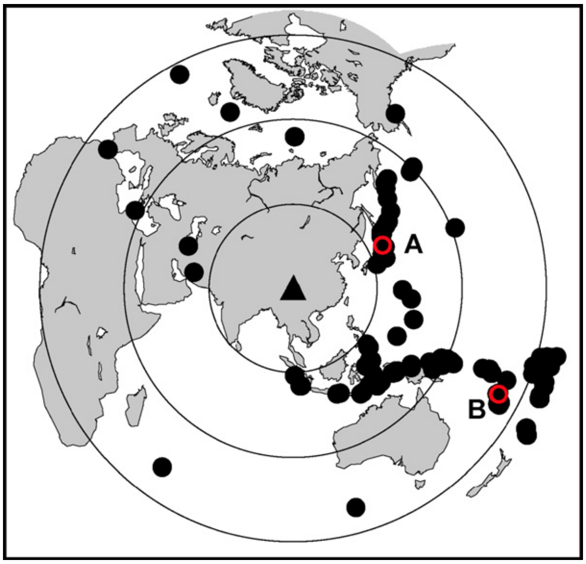

Fig. 3. Azimuthal projection centered on MC08 (black triangle) showing distribution of events used in this study and recorded over the period of September 2003 to October 2004. Small circles mark epicentral distance of 30°, 60°, and 90° from MC08. Two red circles (A and B) indicate regions that saw frequent seismic activity during the recording period (see also Fig. 4).

Station MC22 (24.5°N; 100.2°E) was located in the Sanjiang tectonic unit, to the south of the Red River fault. The 29 receiver functions obtained for this station are plotted in Fig. 4a, for backazimuths between 8° and 253°. Visual inspection reveals a clear P_ms arrival at ∼5 s on all 29 radial receiver functions. Subsequent arrivals include a strong positive one at ∼16 s and a weak negative one at ∼22 s (Fig. 4a). Based on their polarity and relative arrival time, these arrivals could be the free-surface multiples of the Moho, i.e., PpP_ms and PpS_ms (or PsP_ms) phases, respectively (see Fig. 2). In some receiver functions, positive arrivals observed between 9 and 11 s may correspond to P-to-S conversions from upper mantle discontinuities or multiples from intra-crustal discontinuities. Since there are no obvious phases corresponding to P-to-S conversions from an intra-crustal discontinuity, we interpret the arrivals at 9–11 s as P-to-S conversions from structure in the upper mantle (∼80 km). The positive arrival at ∼7 s in the transverse receiver function (thin blue line in Fig. 4b) is likely due to P-to-S conversion from an anisotropic and/or tilted layer, either in the mantle (direct arrival) or in the crust (multiple). There are no prominent phases observed before P_ms (i.e., 5 s) in the transverse receiver function, which indicates that there are no significant effects of anisotropy or tilted layers at shallow depth (Zhang and Langston, 1995; Savage, 1998), which – in turn – implies that our

Table 1
Station information and receiver function results

Station	Latitude (°N)	Longitude (°E)	Number of traces	Moho depth #1 (km)[a]	V_P/V_S ratio[a]	Poisson's ratio[a]	Moho depth #2[b]	Moho depth #3[c]	Category[d]
MC01	31.0	102.3	70	64.0 ± 1.0	1.66 ± 0.03	0.21 ± 0.01	58.6	54.0	2
MC02	30.4	103.4	51	46.0 ± 1.0	1.76 ± 0.08	0.26 ± 0.03	54.2	47.0	1
MC03	30.0	102.5	65	62.0 ± 2.0	1.96 ± 0.05	0.32 ± 0.01	56.6	52.0	2
MC04	30.1	101.5	57	58.0 ± 1.0	1.90 ± 0.06	0.31 ± 0.02	61.0	58.0	2
MC05	30.0	100.2	88 (42)[e]	59.0 ± 1.0	1.76 ± 0.03	0.26 ± 0.01	62.5	60.0	2
MC06	28.9	99.8	57 (24)[e]	64.0 ± 1.0	1.74 ± 0.03	0.25 ± 0.01	61.5	58.0	2
MC07	29.0	100.4	65	58.5 ± 3.5	1.76 ± 0.15	0.25 ± 0.06	61.5	58.5	2
MC08	29.0	101.5	57	52.0 ± 1.0	1.92 ± 0.05	0.31 ± 0.01	56.9	56.0	2
MC09	29.0	102.8	32	49.0 ± 1.0	1.93 ± 0.08	0.31 ± 0.02	51.3	50.0	2
MC10	29.0	103.9	54	40.5 ± 1.5	1.84 ± 0.10	0.29 ± 0.03	48.7	44.0	2
MC11	28.3	103.1	78 (30)[e]	44.0 ± 1.0	1.95 ± 0.07	0.32 ± 0.02	48.2	47.0	2
MC12	27.7	102.2	29	–	–	–	56.7	49.0	3
MC13	27.7	100.8	87	57.0 ± 2.0	1.80 ± 0.05	0.27 ± 0.02	58.5	53.0	2
MC14	27.9	99.7	69	58.0 ± 2.0	1.73 ± 0.07	0.25 ± 0.03	58.6	54.0	2
MC15	26.8	100.0	52	47.0 ± 2.0	1.87 ± 0.08	0.30 ± 0.02	55.1	49.0	2
MC16	27.2	103.6	24	48.5 ± 1.5	1.66 ± 0.07	0.21 ± 0.04	50.9	45.0	2
MC17	26.5	101.7	39	48.5 ± 0.5	1.79 ± 0.06	0.27 ± 0.02	53.0	45.5	2
MC18	26.1	103.2	24	–	–	–	52.6	44.5	3
MC19	25.7	101.9	30	–	–	–	53.0	43.5	3
MC20	25.8	100.6	35	45.5 ± 1.5	1.79 ± 0.08	0.27 ± 0.03	48.1	45.0	2
MC21	25.5	99.6	51	46.0 ± 1.0	1.70 ± 0.06	0.23 ± 0.03	41.3	45.0	2
MC22	24.5	100.2	29	37.5 ± 1.5	1.74 ± 0.10	0.25 ± 0.04	41.3	43.0	1
MC23	24.9	101.5	62	48.0 ± 1.0	1.77 ± 0.07	0.26 ± 0.03	50.9	43.0	2
MC24	24.2	102.8	62	37.0 ± 5.0	1.90 ± 0.18	0.30 ± 0.05	41.6	41.5	1
MC25	24.9	103.7	59	43.5 ± 1.5	1.68 ± 0.10	0.22 ± 0.05	44.6	42.0	2
KMI	25.1	102.7	70 (22)[e]	–	–	–	48.4	43.0	3

[a] Moho depth, V_P/V_S ratio, and Poisson's ratio from this receiver function study.

[b] Moho depth from seismic refraction profiles (Zhu et al., personal communication, 2003).

[c] Moho depth gravity anomaly/deep seismic sounding profile results (Wang et al., 2003).

[d] Measures the reliability of the crustal properties derived from slant-stacking analysis; 1 is highest and 3 is lowest, see text for details.

[e] Total number of traces (events) used for receiver function analysis at each station.

assumption of a 1D crustal velocity structure is adequate.

Station MC05 was located at (30.0°N; 100.2°E), which is in the Songpan-Ganze fold zone. Fig. 4c and d show the processed receiver functions at this station. The initial P-wave pulse is time shifted by ~0.2 s. Such shifts, which have also been observed elsewhere (e.g., van der Meijde et al., 2003), can be attributed to the presence of a low-velocity layer near the surface (i.e., sediments) directly below the station. The arrivals at ~5 and ~7–8 s may correspond to P-to-S conversions from intra-crustal and Moho discontinuities, respectively. Stacking events over all backazimuths can produce slightly broader peaks for P_ms and its multiple phases because of the dependence of the arrival time on backazimuth. Therefore, we stack 42 events from back azimuth range of 104.5°–156.7° (Fig. 4d). For the same reason we bin events for stations MC06, MC11, and KMI (see Table 1). The small-amplitude phases that arrive before the P_ms phases represent P-to-S conversions within the crust. There is a clear positive phase at ~23 s, corresponding to the arrival of PpP_ms, and a negative phase at ~30 s, which corresponds to PpS_ms (or PsP_ms) (Fig. 4c). No prominent phase appears on the transverse receiver function of station MC05 (Fig. 4d).

In contrast to stations MC22 and MC05, some stations have no strong crustal P_ms conversions (Fig. 5). The observation of time delays of the first pulse in receiver functions at most stations indicate that a near-surface low-velocity layer is widely distributed in our study area. The first pulses are complicated due to interference with P-to-S conversions from the bottom of the surface layers, which arrive within ~2 s after the first pulse, e.g., MC02 and MC11 (Fig. 5). At station MC03, which is located just east of the Longmen Shan fault, the radial receiver function waveform has several low-amplitude, positive phases within ~10 s after the first-P arrival. The 10.2-s phase is most probably the P_ms phase because it does not depend on backazimuth and because it is consistent with a Moho depth of ~60 km inferred from refraction studies (Zhu et al., 2003, personal communication), which corresponds to a P_ms phase at >7.0 s assuming an average crustal velocity V_P of < 6.8 km/s and a Poisson's ratio of ≥ 0.25. At station KMI, which is located near N–S trending strike-slip faults (Fig. 1), large-amplitude positive phases are observed at ∼5 s after the main pulse, which could be P_ms. The large variation in the radial receiver functions with backazimuth indi-

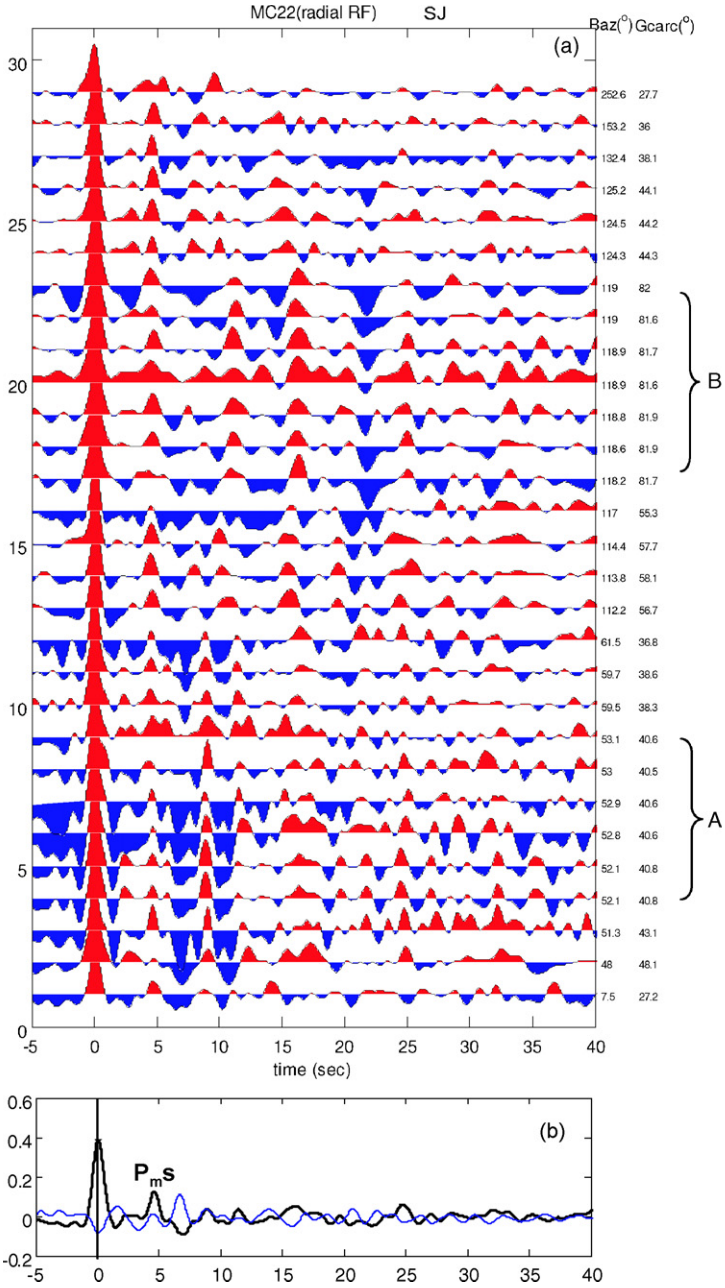

Fig. 4. Receiver functions calculated at stations MC22 (a–b) and MC05 (c–d). (a and c) Waveform sections showing individual, radial receiver functions in the time range spanning 5 s before to 40 s after the direct P arrival. The events are ordered by increasing back azimuth, with back azimuths and epicentral distances for each event shown in the right column. A and B denote clusters of events from Japan and the Fiji-Tonga Islands, respectively (see Fig. 3). (b and d) Radial (thick black line) and transverse (thin blue line) receiver functions obtained by simultaneous deconvolution of all high-quality traces recorded at each station (see Table 1). The traces are moveout corrected for P-to-S conversions occurring between 0 and 500 km depth underneath the stations, with a reference ray parameter of 0.0586 s/km corresponding to earthquakes at ∼67° epicentral distance, and they are filtered using a Gaussian filter with a width of 2.0 Hz.

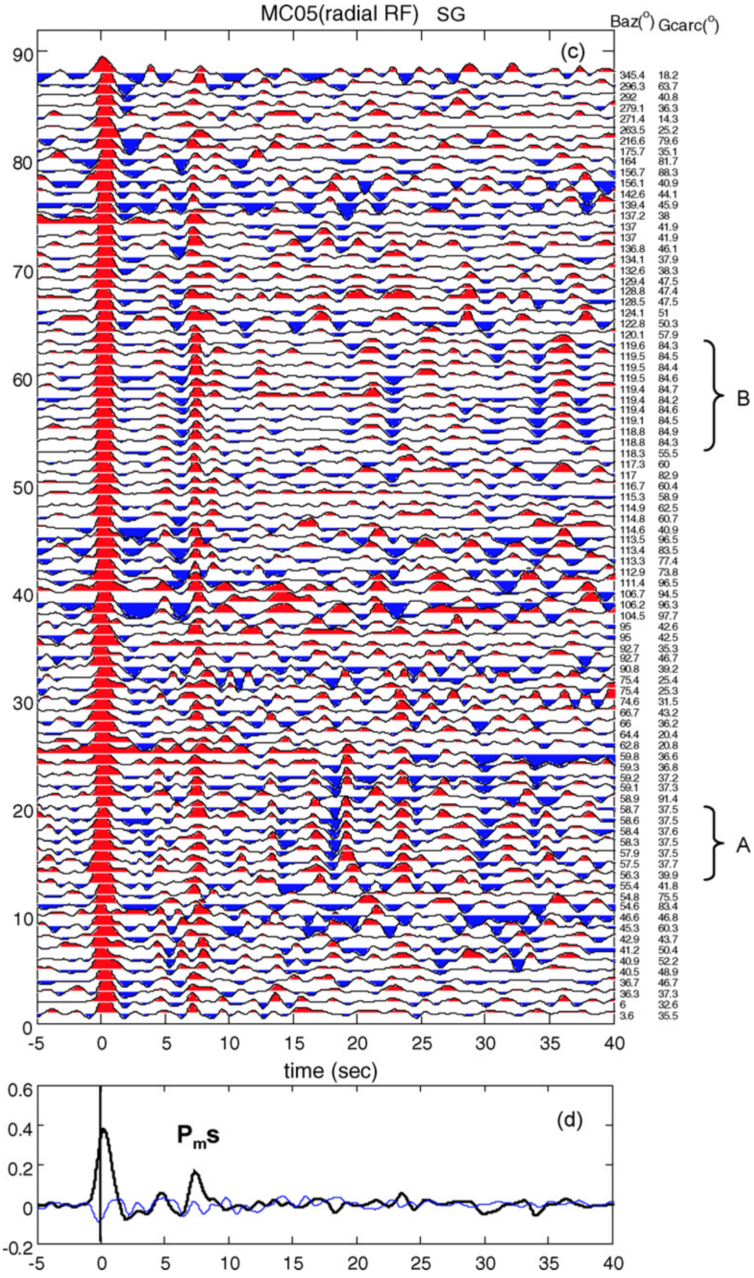

Fig. 4. (*Continued*).

cates a laterally heterogeneous structure beneath station KMI.

4.2. Slant-stacking

We classify stations into three categories depending on the reliability of the derived crustal properties. The first category corresponds to stations for which the P_ms and PpP_ms phases are clearly visible in the radial receiver functions, and for which a clear maximum in the V_P/V_S versus H diagram can be observed even if phase identification is difficult. The second category corresponds to stations with multiple maxima in the V_P/V_S versus H diagram. When identification in the stacks of the maxima corresponding to Moho is ambiguous we use independent estimates of crustal thickness (Wang et al., 2003; Zhu et al, personal communication, 2003) and restrict the average crustal Poisson's ratio to reasonable values

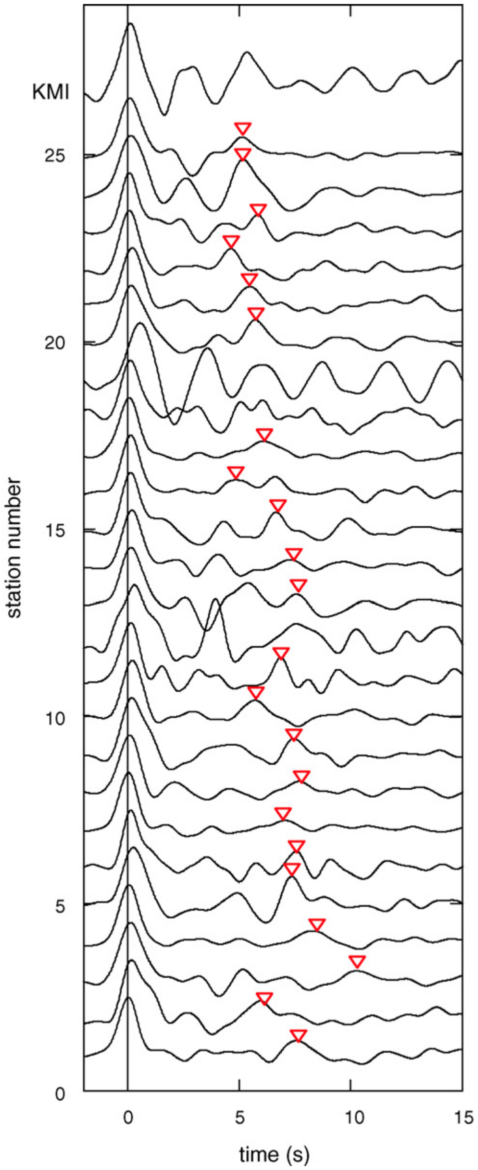

Fig. 5. Radial receiver functions from 25 temporary stations and station KMI obtained by simultaneous deconvolution. P-to-S conversions from the Moho discontinuities are indicated by downward red triangles.

(∼0.25–0.30). The third category corresponds to stations for which the records are too complex or too noisy to determine V_P/V_S and H with sufficient confidence. In this study, we only use stations in the first two categories for further S-wave velocity analysis (Table 1).

Fig. 6a and b show the slant-stacking results from station MC22. The following phases are visible: the P_ms phase at ∼5 s after the first-P arrival, the PpP_ms phase at ∼16 s, and (more tentatively) the PpS_ms (or PsP_ms) phases at ∼22 s. Travel time curves of these phases (thick lines in Fig. 6a) are derived using the combination of H and V_P/V_S that gives the maximum amplitude of the stack. There is only one global maximum in the V_P/V_S versus H diagram, which corresponds to the optimum solution. Therefore, this station is classified in the first category. We obtain a crustal thickness of 37.5 ± 1.5 km and an average crustal Poisson's ratio of 0.25 ± 0.04 beneath this station (Fig. 6b). The inferred crustal thickness of 37.5 km is slightly less than the values of 43 and 41.3 km from previous studies (Wang et al., 2003; Zhu et al., personal communication, 2003; see Table 1). The receiver function study using data from the Yunnan regional seismic network (Hu et al., 2003) yielded a crustal thickness of 36.0 ± 1.0 km at nearby station YX (24.3°N, 100.1°E). Hu et al. (2003) also derived a Poisson's ratio of 0.31 ± 0.01, which is larger than but not incompatible with our estimate of 0.25 ± 0.04.

Station MC05 has local maxima in addition to a global maximum in the V_P/V_S–H diagram (Fig. 6c–d). One of the local maxima yields H = 42.5 km and Poisson's ratio of 0.33, whereas the global maximum corresponds to a crustal thickness of 59.0 ± 1.0 km and average crustal Poisson's ratio of 0.26 ± 0.01. Because seismic refraction data suggest a thickness of ∼62.5 km (Zhu, 2003, personal communication) we select the latter values for crustal thickness (i.e., 59.0 ± 1.0 km) and Poisson's ratio (i.e., ∼0.26) at station MC05.

The receiver function waveforms from stations MC12, MC18, and MC19 are too noisy to identify the P_ms phase among several pulses with similar amplitude (Fig. 5). They are in the third category and thus not included in further analysis.

The slant-stacking analysis reveals that the depth to the Moho changes gradually across our array, from ∼37 km in Yunnan province to ∼64 km below eastern Tibet. The average crustal Poisson's ratio varies between 0.21 and 0.32 and is the lowest in the southern Yangtze platform. The Poisson's ratio is the highest, with values consistently above 0.30, below the eastern margin of the Tibetan Plateau just west of the Sichuan basin (below the latter the Poisson's ratios are generally less than 0.29). The Songpan-Ganze fold zone, the region of high average elevation (∼4 km), has a thick crust. Station MC01, situated between the Xianshuihe and Longmen Shan faults, has the thickest crust (i.e., 64 ± 1.0 km) and a small Poisson's ratio (i.e., 0.21 ± 0.1). On the Yangtze platform, MC02 and MC10 sample the western Sichuan basin (Fig. 1). Here, the crust thickness is between ∼46 and 41 km, and the Poisson's ratio is between ∼0.26 and 0.29. The crust-mantle boundary of the Yangtze platform deepens northwestward from ∼40 to 56 km. The Poisson's ratio generally decreases eastward from ∼0.30 to

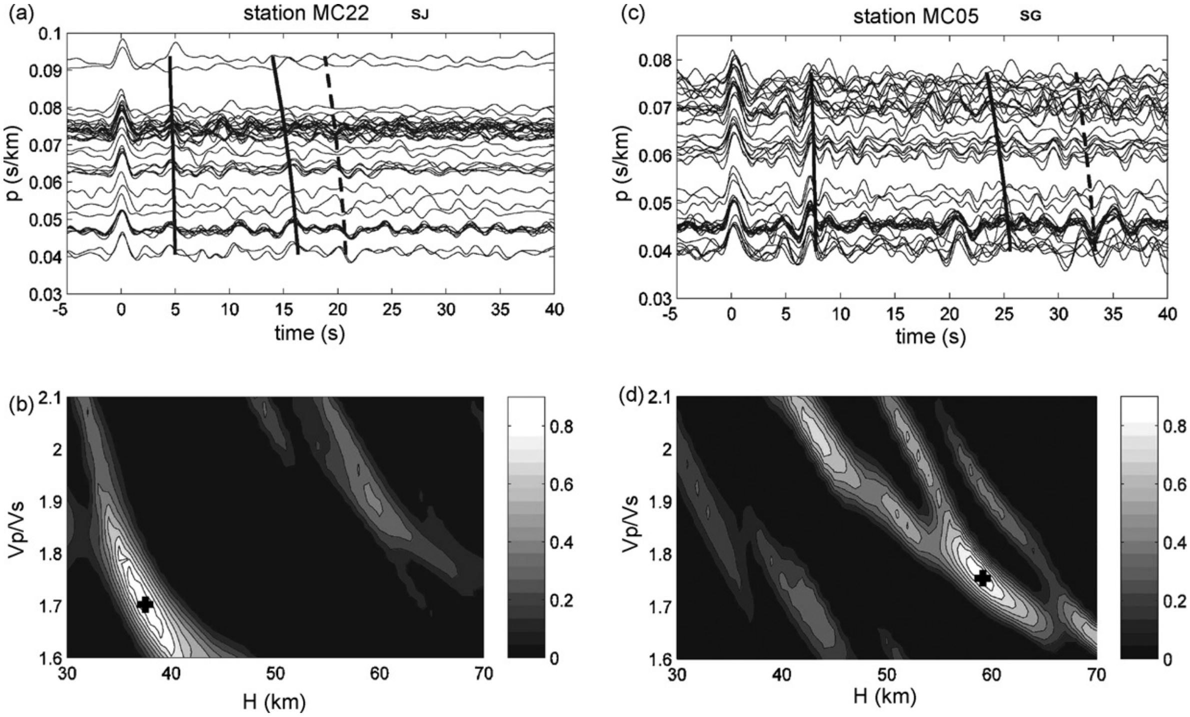

Fig. 6. Slant-stacking results for stations MC22 and MC05. (a and c) Receiver functions ordered by ray parameter (*p*) for station MC22 and MC05, respectively, along with predicted travel time curves estimated from the optimum solution of *H* and V_P/V_S, determined by slant-stacking analysis ($V_P = 6.2$ km/s). These curves (dashed for arrivals that are more tentative) were generated using a simple, flat-Earth, and one-layer crust model. (b and d) Solution surfaces constructed by a direct search over V_P/V_S vs. *H* space. The optimum solution is indicated by a cross; contour lines are spaced at intervals of 0.1. Scale is normalized and all solutions with negative sum are shaded black.

0.22. The Sanjiang fold zone, west of the Red River fault, has a crustal thickness of ∼38–46 km and Poisson's ratio of ∼0.23–0.25.

4.3. S-wave velocity profiles

S-wave velocity profiles derived from least-squares inversion and grid search through simplified models are show in Fig. 7 (for eight stations) and in Fig. A11, Appendix II in Supplementary data (all stations). Low-velocity zones are identified as velocity minima on smoothed crustal velocity models beneath many stations in the southeastern part of the Tibetan Plateau. The thickness of the near-surface low-velocity layer (S-LVL) varies from ∼0 to 10 km. An intra-crustal low-velocity layer (IC-LVZ) is mostly observed in the Songpan-Ganze fold zone and the western Yangtze platform. On average, the S-wave velocity in the IC-LVZ is ∼0.5–0.8 km/s lower than that of its overlying layer. Both S-LVL and IC-LVZ are robust features: S-LVLs are well constrained by a ∼0.2-s time shift of the incident P-wave pulse; IC-LVZs are only assigned to stations where a low-velocity layer is required both in the least-squares solution and in the simplified model to fit the measured receiver function waveform (see Appendix I in Supplementary data).

4.3.1. Songpan-Ganze fold zone (SG)

At station MC01, the receiver function synthesized from the derived S-wave velocity profile matches the observed data within the observational uncertainty (Fig. 7). The 68-km thick crust has a 20-km thick upper crust with S-wave velocity of ∼3.7 km/s and a 30-km lower crust with S-wave velocity of 3.9 km/s. There is a low-velocity zone at ∼20–40 km which is necessary to explain the negative arrival at ∼2.6 s in the receiver function waveform. Our results are consistent with previous S-wave tomography, which yielded a small negative velocity anomaly at ∼50 km beneath this station (Wang et al., 2003). Stations MC04 and MC08 have similar velocity structures: there are no obvious low-velocity layers near the surface and the S-wave velocities in the upper and middle crust are more or less constant. The 57-km thick crust at MC04 consists a ∼32-km upper crust with S-wave velocity of 3.2 km/s and 25-km lower crust with S-wave velocity of 3.5 km/s.

Stations MC05-07 have very similar S-wave velocity profiles. These stations are marked by an IC-LVZ

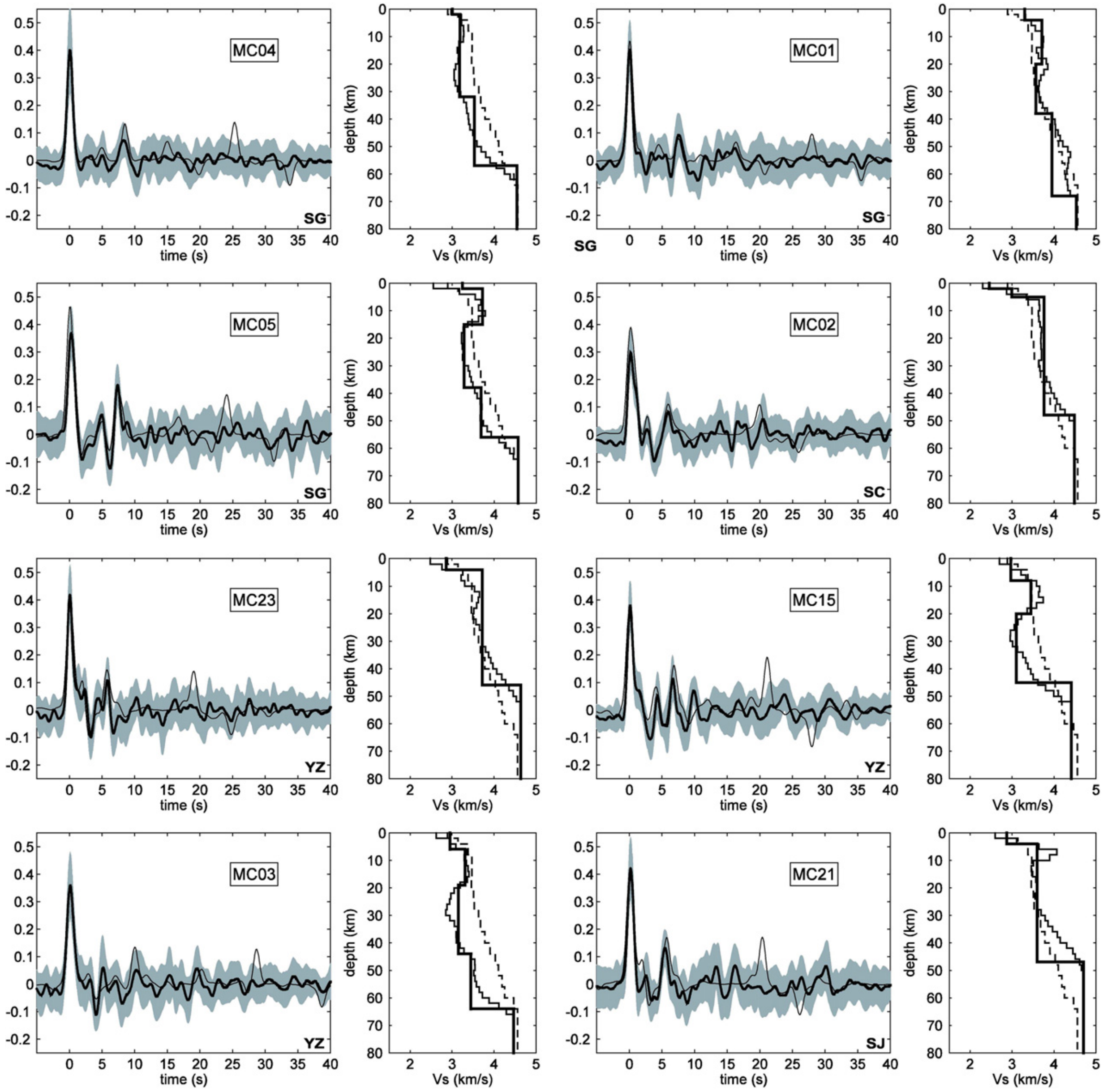

Fig. 7. Least-squares inversion and grid-search (i.e. simplified modeling) results for eight stations. Results for each station are shown in two panels. The left panel shows the observed receiver function (thick black lines), its standard deviation (±σ) bounds (grey shading), and the synthetic receiver function corresponding to the grid-search solution (thin black line). The right panel shows the initial model (thin dashed lines), the preferred solution (thin black lines) from many-layered least-squares inversion, and the grid-search solution (thick black line). Results for all stations are presented in Figure A11 in Supplementary data.

with S-wave velocity of ∼3.3 km/s. The IC-LVZ extends between ∼15 and 38 km depth at station MC05 (Fig. 7), which is necessary to explain the negative phases at ∼2 and 6 s in the receiver function waveform (see Appendix I in Supplementary data). In the same region, MT studies show a high conductive layer below ∼10 km (Sun et al., 2003), and S-wave tomography shows a low-velocity anomaly between ∼10–30 km depth (Wang et al., 2003). The positive velocity gradient at ∼30 km corresponds to the 5-s arrival in the receiver function waveform, which can be related to the Conrad discontinuity (i.e., ∼25 km depth) inferred from deep seismic sounding (Wang et al., 2003). We note that the strong Moho multiples that appear near ∼23 and ∼31 s in the synthetic waveforms calculated from the preferred velocity model are not clearly visible in the stacked receiver functions (Fig. 7).

This discrepancy is due in large part to the fact that receiver functions are stacked using moveout curves that account for variations in relative travel time of direct conversions, but that do not stack multiples coherently.

4.3.2. *Yangtze platform (YZ)*

Two stations sample the crust of the western Sichuan basin. Beneath station MC02, the S-LVL is ∼5 km thick, which is consistent with the layers of Mesozoic sediments in the Sichuan basin (Kirby et al., 2000). The crust there has a thickness of 48 km and exhibits a fairly uniform S-wave velocity (average ∼3.7 km/s) below the S-LVL. In contrast, station MC10 has an IC-LVZ at ∼10–20 km with S-wave velocity of ∼3.1 km/s.

In the western Yangtze platform, stations MC17, MC20, and MC23 have similar S-wave velocity profiles, without obvious IC-LVZs. Stations MC13 and MC15 have IC-LVZs with S-wave velocities of ∼3.1 km/s. A similar IC-LVZ has been inferred from other receiver function studies (Hu et al., 2003; He et al., 2004), except for a station at (26.9°N, 100.2°E), which is close to station MC15, where an IC-LVZ has not been previously observed (Hu et al., 2003). Stations MC03, MC09, MC11, MC16, MC25, and MC24 sample the Yangtze platform from north to south. Their S-wave velocity profiles are significantly different. Station MC03, located near the Longmen Shan fault, reveals an IC-LVZ at ∼20–44 km and two velocity discontinues at ∼44 and 64 km (corresponding to the arrivals at ∼5.2 and 10.1 s in the receiver function waveform). These can be interpreted as intra-crustal and Moho discontinuities, respectively. Station MC09 has an IC-LVZ at ∼15–30 km, with an S-wave velocity of ∼3.2 km/s. Stations on the southern Yangtze platform do not show evidence for IC-LVZs. Our results generally agree with previous receiver function studies in southern Tibet (Hu et al., 2003; He et al., 2004).

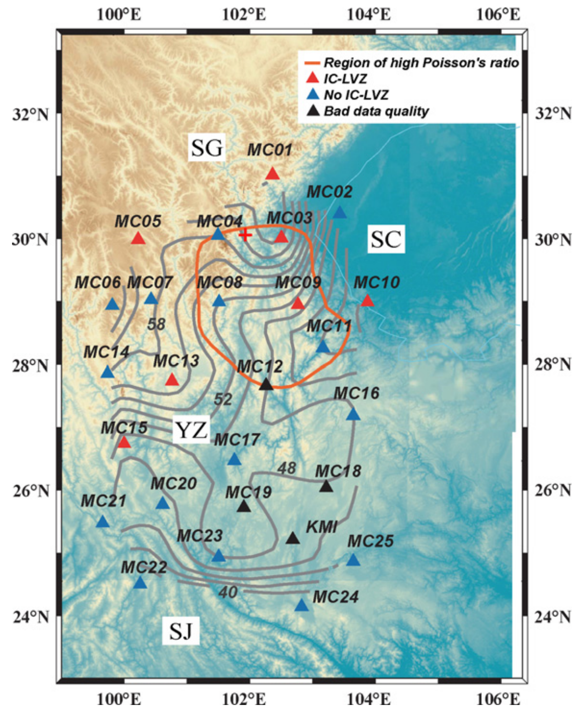

Fig. 8. Contour map of crustal thickness (in km) from this receiver function study. The orange line denotes the region of high Poisson's ratio (>0.30). The red triangles represent stations with an obvious IC-LVZ, the blue ones represent stations without obvious IC-LVZ, and the black ones represent stations without sufficient data quality. The Sichuan basin is outlined by a thin blue line. Tectonic labels are the same as in Fig. 1.

4.3.3. *Sanjiang fold system (SJ)*

Stations MC21 and MC22 sample the Sanjiang fold system, west of the Red River fault. MC21 is located to the east of the Tengchong volcanic area. The crust deepens northward by ∼9 km from station MC22 to station MC21. There is no obvious IC-LVZ and intra-crustal discontinuities at both stations. Similar receiver function results were observed by Hu et al. (2003) in the Sanjiang fold system.

5. Discussion

5.1. *Crustal thickness*

The crustal thickness varies between 37 and 64 km in SE Tibet and its surrounding area (Fig. 8). The thickness of the crust is large beneath the Songpan-Ganze fold zone (∼60 km) and decreases eastward to the western Sichuan basin (∼46 km) and southeastward to the Yangtze platform (∼40 km). The crust beneath the Sanjiang fold zone has a thickness of ∼38–46 km.

In general, the Moho depths derived in our study are consistent with previous results (e.g., Li and Mooney, 1998; Hu et al., 2003; Wang et al., 2003; He et al., 2004). Specifically, Fig. 9 (also Table 1) shows that for realistic values of the average crustal P-wave velocity (6.2–6.4 km/s) our results agree well with estimates from seismic refraction profiles (Zhu et al., personal communication, 2003) or Bouguer gravity anomaly and deep seismic sounding profiles data (Wang et al., 2003). The correlation coefficients between our Moho depth values and their estimates are 0.88 and 0.86, respectively. The only significant outliers are stations MC01 and MC03, for which we obtained thicker crust (Table 1). When we include these outliers, the root mean square of the differences between our results and those from the inde-

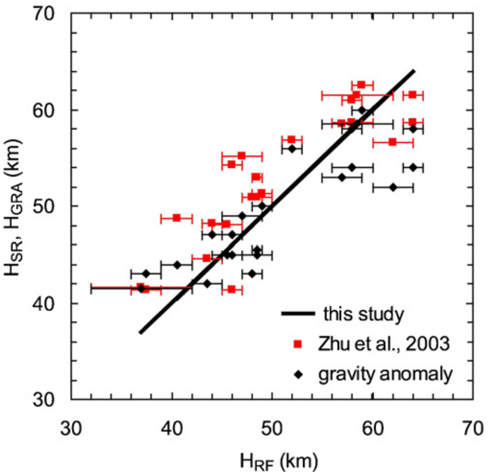

Fig. 9. Comparison between crustal thicknesses obtained in this study, H_{RF}, and those from previous seismic refraction, H_{SR}, and gravity anomaly and deep seismic sounding profile data, H_{GRA} (Zhu et al., 2003, personal communication; Wang et al., 2003). Correlation coefficients are 0.88 between H_{RF}–H_{SR} and 0.86 between H_{RF}–H_{GRA}.

pendent studies are about 4 km. Some of this difference can be due to the fact that the receiver function analysis and the seismic refraction study sample the crust at different locations and that the spatial resolution of two methods is different (Chevrot and van der Hilst, 2000).

Fig. 10 shows the S-velocity profile along an east–west cross section (line 1 in Fig. 1) beneath the northern part of our study region, adjacent to the Sichuan basin; the topographic slope across the east margin of the Tibetan Plateau (Fig. 10, top) is steep and the elevation decreases by ~3500 m over a lateral distance of 150 km. The steep topographic gradient in the western Sichuan basin was interpreted by Clark et al. (2005) to be a result of crustal material flowing around the strong lithosphere of the Sichuan block in the channel flow model. From station MC05 – on the plateau proper – to station MC02 – in Sichuan basin – the base of the crust shallows by 9.5 ± 2.0 km and the elevation decreases by ~3500 m. An Airy isostatic model predicts a change in crustal thickness of ~24 km (Braitenberg et al., 2000), which suggests that crustal material may still be piling up at the east margin of the Tibetan Plateau. Along Line 2 (Fig. 11), which transects the southeastern margin of the Tibetan Plateau, the average topographic slope is smaller than that across the eastern margin (line 1). The crust shallows southeastward by 19.7 ± 6.0 km with a change in elevation of ~2300 m, in agreement with an Airy iso-

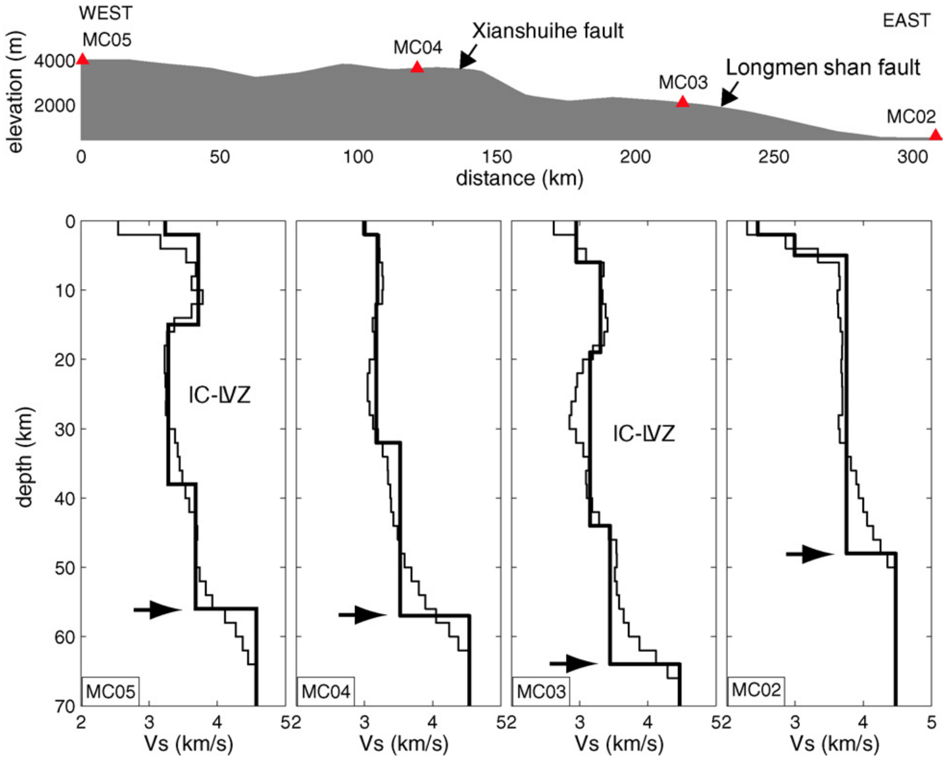

Fig. 10. Elevation and velocity cross-sections along Line 1 in Fig. 1. Top: topography profile and (projected) locations of the stations (red triangles) and major fault zones. Bottom: S-wave velocity models (IC-LVZ = intra-crustal low-velocity zone). The Moho depth (inferred from slant-stacking analysis) is indicated by black arrows.

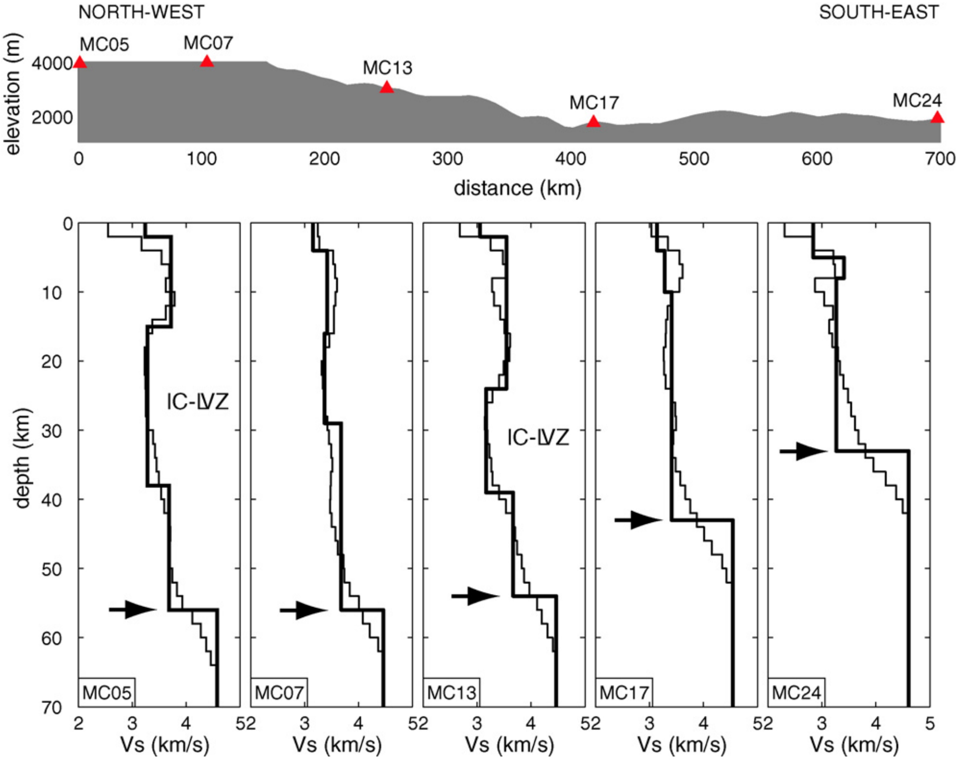

Fig. 11. Same as Fig. 10 but for Line 2 in Fig. 1.

static model. Our result of Moho compensation using the Airy isostatic model (Braitenberg et al., 2000) is consistent with previous gravity anomaly studies, which indicated that the topography of the southeastern part of the Tibetan Plateau is locally compensated except for the eastern margin across the Longmen Shan fault on to the western Sichuan basin (Jiang and Jin, 2005; Jordan and Watts, 2005).

5.2. Poisson's ratio and (average) crustal composition

Poisson's ratios can help constrain crustal mineralogy and chemical composition. Mineral physics and field constraints indicate that (1) the Poisson's ratio increases more-or-less linearly with decreasing SiO_2 content for continental crust and (2) high ratios (>0.30) suggest the existence of partial melt (Christensen, 1996; Owens and Zandt, 1997), especially if the perturbation in Poisson's ratio is localized to an intra-crustal layer (see Appendix III in Supplementary data). We interpret the large range of observed Poisson's ratio (0.22–0.32) in the southeastern part of the Tibetan Plateau to be a result of heterogeneity in crustal composition and, locally, the existence of partial melt.

Most of our study region has an intermediate-to-high Poisson's ratio (>0.25) except for a few stations in the southern Yangtze platform. The ratio is highest (>0.30) in the eastern margin of the Tibetan Plateau, just west of the Sichuan basin (Fig. 8). In the Yangtze platform, Poisson's ratios generally decrease eastward, from ~0.30 to 0.22. The normal-to-high values in the western Yangtze platform (~0.26–0.30) are consistent with a mafic/ultramafic lower crust as inferred from recent geophysical surveys (Xu et al., 2001), and may indicate the presence of partial melt in the crust, whereas low-to-intermediate values suggest a felsic-to-intermediate composition in the southern Yangtze platform. The ratios in the Sanjiang fold system (~0.23–0.25) are consistent with results from seismic refraction studies and suggest an "average" crustal composition (Kan et al., 1986; Li and Mooney, 1998).

Hu et al. (2003) estimated Poisson's ratios – using Eqs. (1) and (2) – from differential travel times of P_ms and PpP_ms phases at 23 temporary stations in Yunnan province. They showed that the western Yangtze platform has Poisson's ratios of 0.30–0.35, which are higher than our values of 0.26–0.30. This discrepancy may, in part, be due to differences in data and methodology. Our results are consistent with Zurek et al. (2007, personal communication), who used a slant-stacking method similar to the one deployed here.

5.3. Low-velocity zones

Our results suggest the presence of complex 3D heterogeneity in the crust beneath SE Tibet. The most prominent features in the S-wave velocity profiles presented here are the near-surface and intra-crustal low-velocity zones (Figs. 7, 10, and 11). The quasi-ubiquitous S-LVL can be related to the surface sedimentary basins (Leloup et al., 1995; Song and Lou, 1995; Burchfiel and Wang, 2003). The IC-LVZ is widely observed in the study region, but with significant lateral variation in its depth and strength. In some places the IC-LVZ corresponds to the middle crust, but in other places it marks the lower crust. In general, it becomes thinner toward the Sichuan basin and is absent in the southern part of the Yangtze platform (Fig. 8). Compared to the shallow crust, the reduction of the S-wavespeed in IC-LVZ is in the range of ∼12–19%.

The existence of IC-LVZs as inferred here is generally consistent with results from seismic sounding, seismic tomography, and previous receiver function analyses (e.g., Li and Mooney, 1998; Huang et al., 2002; Wang et al., 2003; Hu et al., 2003; He et al., 2004; Yao et al., submitted). Along line 1 (Fig. 10), the IC-LVZ also coincides with one or more intra-crustal layers of high (electric) conductivity inferred from MT data (Sun et al., 2003).

5.4. Partial melt?

Earthquake focal depths and heat flow studies both indicate a relatively high geothermal gradient in the southeastern part of the Tibetan Plateau (Sun et al., 2004; Wu et al., 1988; Hu et al., 2000). In crystalline continental crust, seismic velocities generally increase with increasing depth. However, wavespeed reductions can occur in regions with steep geothermal gradients (e.g., Kern and Richter, 1981; Kono et al., 2006) and, in particular, in regions of partial melt (Meissner, 1986). In view of (i) the magnitude of the reduction in shear wavespeed in the IC-LVZs, (ii) the high average Poisson's ratios of the crust and their possible translation into vertically localized perturbations (see Appendix III in Supplementary data), (iii) the correlation with a zone of high conductivity inferred from the inversion of MT data, and (iv) the association with high heat flow, we suggest that crustal partial melt exists beneath parts of the eastern margin of the Tibetan Plateau, possibly with continuation into the northwesternmost part of the Yangtze platform.

In general, the S-wave velocity decreases and Poisson's ratio increases drastically when the temperature approaches and exceeds the solidus. Mueller and Massonne (2001) suggested that for typical mid-crustal pressures, granite starts to melt at ∼650 °C. If we suppose a similar composition, the inferred Poisson's ratio of > 0.30 and S-wave velocity of ∼3.0–3.2 km/s in the IC-LVZ (∼10–30 km in depth) indicate a temperature of ∼700–800 °C and an amount of melt less than 4%. This interpretation is consistent with inferences from receiver function studies in northern Tibet (Zhu et al., 1995) and with Roger et al. (1995), who suggested that the young Konga Shan granite (∼10 Ma) at the southern segment of the Xianshuihe fault (Fig. 1) might have originated from partial melting of continental crust. However, our results suggest that partial melt is restricted to certain geographical regions (that is, the data do not require it for large parts of our study region) and that it involves the middle or the lower crust, and perhaps, in some locations, both (see also, Yao et al., submitted).

Previous geological and experimental studies (Leloup et al., 1995; Rabinowicz and Vigneresse, 2004) suggested that crustal partial melt may be partly due to shear heating in southeastern Tibet. Another contribution may come from the upper-mantle decompression melting which also contributed to the young volcanism (Wang et al., 2001). Intra-crustal zones of partial melt in northern Tibet have been attributed to the extrusion of mantle-derived magma (e.g., Zhu et al., 1995; Nelson et al., 1996; Kind et al., 2002). Furthermore, a shallow IC-LVZ (∼10–20 km) around the Tengchong volcano was interpreted by Wang and Gang (2004) to be the result of upper-mantle magma activity and heat conduction through the near vertical fault.

Since the viscosity of crustal rocks decreases with increasing fraction of partial melt (Bagdassarov and Dorfman, 1998), it is tempting to associate the IC-LVZ with a mechanically weak zone. This would be consistent with a model in which crustal shortening is accommodated by channel flow in the mid-to-lower crust (Royden et al., 1997; Clark and Royden, 2000; Roy and Royden, 2000a,b; Clark et al., 2005). Insofar, as the association of IC-LVZs with layers of weaker rheology is correct, the results from receiver function analysis (this study) and from surface wave array tomography (Yao et al., submitted) suggest that there is substantial lateral variation in existence, strength, and position (i.e., depth range) of such zones. In turn, this suggests a complex 3D geometry of intra-crustal channel flow.

6. Summary

By analyzing receiver functions from 25 temporary seismograph stations, we estimated the crustal velocity structure in the southeastern margin of the Tibetan Plateau. The crust varies in thickness from ∼60 km in the Songpan-Ganze fold system to ∼40 km in the southern Yangtze platform. The gradient of the Moho discontinuity is the greatest in the eastern margin of Tibet toward the western Sichuan basin. The crustal thickness generally follows the Airy isostatic model except toward the western Sichuan basin, which indicates that crustal material may still be piling up at the eastern margin of the Tibetan Plateau. Poisson's ratio varies greatly in our study region. The western Yangtze platform exhibits intermediate-to-high Poisson's ratios (>0.26), which can be related to the existence of high-velocity lower crust with a mafic/ultramafic composition and, locally, to the presence of partial melt. In general, the overall crustal chemical composition varies between felsic and intermediate.

Arguably, the most conspicuous features in the velocity profiles derived here are the pronounced low-velocity zones in the crust. The geometry may not be well resolved, but these IC-LVZs are required by the data (the starting models used for the inversions do not have clear low-velocity structures in the crust (Fig. 7)). An IC-LVZ is widely observed in the study region, but with significant lateral variation in its depth and strength. It becomes thinner toward the Sichuan basin and is absent in the southern part of the Yangtze platform (Fig. 8). The S-wavespeed reduction in IC-LVZ is ∼12–19% relative to the shallow crust. As seismic velocities generally increase with increasing depth in crystalline continental crust, we infer the possible existence of crustal partial melt in IC-LVZ. Our interpretation is supported by observations of crustal high-conductivity layers and high heat flow values in our study area (e.g., Wang and Huang, 1988; Hu et al., 2000; Sun et al., 2003) and by inferences from high-resolution surface wave tomography (Yao et al., submitted). Collectively, these observations indicate that the low-viscosity zone in the crust of the central Tibetan Plateau probably extends into southeastern Tibet. The substantial lateral variations in the existence, character, strength, and position of IC-LVZ may point to intra-crustal channel flow but with a complex 3D geometry.

Acknowledgements

We thank Prof. Z. Chen at the Chengdu Institute of Geology and Mineral Resources for the excellent organization of the field component of our array studies in Sichuan and Yunnan provinces, SW China. We acknowledge Prof. J. Zhu for providing us the crustal velocity models. We benefited from the constructive discussion with Leigh Royden and Christopher Studnicki-Gizbert. We thank Charles Ammon and Andrew Frederiksen for providing inversion and forward modeling codes. We are grateful for the constructive comments by the Editor, George Helffrich, which have helped improve the manuscript. This research was supported by NSF's Continental Dynamics program under grant EAR 0003571.

Appendix A. Supplementary data

Supplementary data associated with this article can be found, in the online version, at doi:10.1016/j.pepi.2007.09.002.

References

Ammon, C., Randall, G., Zandt, G., 1990. On the non-uniqueness of receiver function inversions. J. Geophys. Res. 95, 15303–15318.

Avouac, J.P., Tapponnier, P., 1993. Kinetic model of active deformation in central-Asia. Geophys. Res. Lett. 20, 895–898.

Bagdassarov, N., Dorfman, A., 1998. Granite rheology: magma flow and melt migration. J. Geol. Soc. 155, 863–872.

Berteussen, K.A., 1977. Moho depth determinations based on spectral ratio analysis of NORSAR long-period P waves. Phys. Earth Planet. Int. 31, 313–326.

Bostock, M.G., 1998. Mantle stratigraphy and evolution of the Slave Province. J. Geophys. Res. 103, 21183–21200.

Braitenberg, C., Zadro, M., Fang, J., Wang, Y., Hsu, H.T., 2000. The gravity and isostatic Moho undulations in Qinghai-Tibet Plateau. J. Geodyn. 30 (5), 489–505.

Burchfiel, B.C., Wang, E.C., 2003. Northwest-trending, middle Cenozoic, left-lateral faults in southern Yunnan, China, and their tectonic significance. J. Struct. Geol. 25 (5), 781–792.

Burchfiel, B.C., Chen, Z., Liu, Y., Royden, L.H., 1995. Tectonics of the Longmenshan and adjacent regions, central China. Int. Geol. Rev. 37 (8), 661–735.

Chen, B.W., Wang, K.W., Liu, W.X., 1987. Geotectonics in Nujiang-Lancangjiang-Jinshajiang Region (in Chinese). Geol. Publ., Beijing, 204 pp.

Chen, Z., Burchfiel, B.C., Liu, Y., King, R.W., Royden, L.H., Tang, W., Wang, E., Zhao, J., Zhang, X., 2000. Global Positioning System measurements from eastern Tibet and their implications for India/Eurasia intercontinental deformation. J. Geophys. Res. 105 (B7), 16215–16227.

Chevrot, S., van der Hilst, R.D., 2000. The Poisson ratio of the Australian crust: geological and geophysical implications. Earth Planet. Sci. Lett. 183 (1/2), 121–132.

Christensen, N.I., 1996. Poisson's ratio and crustal seismology. J. Geophys. Res. 101 (B2), 3139–3156.

Clark, M.K., Royden, L.H., 2000. Topographic ooze: building the eastern margin of Tibet by lower crustal flow. Geology 28 (8), 703–706.

Clark, M.K., Bush, J.W.M., Royden, L.H., 2005. Dynamic topography produced by lower crustal flow against rheological strength heterogeneities bordering the Tibetan Plateau. Geophy. J. Int. 162, 575–590.

Flesch, L.M., Holt, W.E., Silver, P.G., Stephenson, M., Wang, C.Y., Chan, W.W., 2005. Constraining the extent of crust-mantle coupling in central Asia using GPS, geologic, and shear-wave splitting data. Earth Planet. Sci. Lett. 238 (1/2), 248–268.

Frederiksen, A.W., Folsom, H., Zandt, G., 2003. Neighbourhood inversion of teleseismic Ps conversions for anisotropy and layer dip. 155 (1), 200–212.

Gurrola, H., Baker, G.E., Minster, J.B., 1995. Simultaneous time-domain deconvolution with application to the computer of receiver functions. Geophys. J. Int. 120, 537–543.

He, Z.Q., Ye, T.L., Su, W., 2004. S-wave velocity structure of the middle and upper crust in the Yunnan region, Chinese (in Chinese). J. Geophys. 47 (5), 838–844.

Hetland, E.A., Wu, F.T., Song, J.L., 2004. Crustal structure in the Changbaishan volcanic area, China, determined by modeling receiver function. Tectonophysics 386, 157–175.

Holt, W.E., 2000. Correlated crust and mantle strain fields in Tibet. Geology 28 (1), 67–70.

Hu, S.B., He, L.J., Wang, J.Y., 2000. Heat flow in the continental area of China: a new data set. Earth Planet. Sci. Lett. (2), 407–419.

Hu, J.F., Su, Y.J., Zhu, X.G., Chen, Y., 2003. S-wave velocity and Poisson's ratio structure of crust in Yunnan and its implication (in Chinese). Sci. China B 48 (2), 210–218.

Huang, J.L., Zhao, D.P., Zheng, S.H., 2002. Lithospheric structure and its relationship to seismic and volcanic activity in southwest China. J. Geophys. Res. 107 (B10), 2255, doi:10.1029/2000JB0000137.

Jiang, X.D., Jin, Y., 2005. Mapping the deep lithospheric structure beneath the eastern margin of the Tibetan Plateau from gravity anomalies. J. Geophys. Res. 110, B07407, doi:10.1029/2004JB003394.

Jordan, T.A., Watts, A.B., 2005. Gravity anomalies, flexure and the elastic thickness structure of the India–Eurasia collisional system. Earth Planet. Sci. Lett. 236 (3/4), 732–750.

Kan, R.J., Hu, H.X., Zeng, R.S., Mooney, W.D., McEvilly, T.V., 1986. Crustal structure of Yunnan province, Peoples-Republic-of-China, from seismic refraction profiles. Science 234 (4775), 433–437.

Kern, H., Richter, A.E., 1981. Temperature derivates of compressional and shear wave velocities in crustal and mantle rocks at 6 Kbar confining pressure. J. Geophys. 49 (1), 47–56.

Kind, R., Kosarev, G.L., Petersen, N.V., 1995. Receiver functions at the stations of the German regional seismic network (GRSN). Geophys. J. Int. 121 (1), 191–202.

Kind, R., Ni, J.F., Zhao, W.J., Wu, J.X., Yuan, X.H., Zhao, L.S., Sandvol, E., Reese, C., Nabelek, J., Hearn, T., 1996. Evidence from earthquake data for a partially molten crustal layer in southern Tibet. Science 274, 1692–1694.

Kind, R., Yuan, X., Saul., J., Nelson, D., Sobolev, S.V., Mechie, J., Zhao, W., Kosarev, G., Ni, J., Achauer, U., Jiang, M., 2002. Seismic images of crust and upper mantle beneath Tibet: evidence for Eurasian plate subduction. Science 298, 1219–1221.

King, R.W., Shen, F., Burchfiel, B.C., Royden, L.H., Wang, E., Chen, Z., Liu, Y., Zhang, X.Y., Zhao, J.X., Li, Y., 1997. Geodetic measurement of crustal motion in southwest china. Geology 25, 179–182.

Kirby, E., Whipple, K.X., Burchfiel, B.C., Tang, W.Q., Berger, G., Sun, Z.M., Chen, Z.L., 2000. Neotectonics of the Min Shan, China: implications for mechanisms driving Quaternary deformation along the eastern margin of the Tibetan Plateau. Geol. Soc. Am. Bull. 112 (3), 375–393.

Kono, Y., Ishikawa, M., Arima, M., 2006. Laboratory measurements of P- and S-wave velocities in polycrystalline plagioclase and gabbronorite up to 700 °C and 1 GPa: implications for the low velocity anomaly in the lower crust. Geophys. Res. Lett. 33, L15314, doi:10.1029/2006GL026526.

Langston, C.A., 1979. Structure under Mount Rainier, Washington, inferred from teleseismic body waves. J. Geophys. Res. 84, 4749–4762.

Leloup, P.H., Lacassin, R., Tapponnier, P., Schärer, U., Zhong, D.L., Liu, X.H., Zhang, L.S., Ji, S.C., Trinh, P.T., 1995. The Ailao Shan-Red River shear zone (Yunnan, China), tertiary transform boundary of IndoChina. Tectonophysics 251, 3–84.

Lev, E., Long, M.D., van der Hilst, R.D., 2006. Seismic anisotropy in Eastern Tibet from shear-wave splitting reveals changes in lithospheric deformation. Earth Planet. Sci. Lett. 251 (3/4), 293–304.

Li, S., Mooney, W.D., 1998. Crustal structure of China from deep seismic sounding profile. Tectonophysics 288, 105–113.

Lin, Z., Hu, H., Zhang, W., 1993. The preliminary interpretation of deep seismic sounding in western Yunnan (in Chinese). Acta Seismol. Sin. 15 (4), 282–295.

Lodge, A., Helffrich, G., 2006. Depleted well root beneath the Cape Verde Islands. Geology 34 (6), 449–452.

Mavko, G.M., 1980. Velocity and attenuation in partially molten rocks. Geophys. J. Int. 85, 5173–5189.

McNamara, D.E., Owens, T.J., Silver, P.G., Wu, F.T., 1994. Shear wave anisotropy beneath the Tibetan Plateau. J. Geophys. Res. 99 (B7), 13655–13665.

Meissner, R., 1986. The continental crust; a geophysical approach. Int. Geophys. Ser. 34, 426 pp.

Molnar, P., Tapponnier, P., 1975. Cenozoic tectonics of Asia: effect of a continental collision. Science 189, 419–426.

Mueller, H.J., Massonne, H.J., 2001. Experimental high pressure investigation of partial melting in natural rocks and their influence on V_P and V_S. Phy. Chem. Earth (A) 26 (4/5), 325–332.

Nelson, K.D., Zhao, W.J., Brown, L.D., Kuo, J., Che, J.K., Liu, X.W., Klemperer, S.L., Makovsky, Y., Meissner, R., Mechie, J., Kind, R., Wenzel, F., Ni, J., Nabelek, J., Chen, L.S., Tan, H.D., Wei, W.B., Jones, A.G., Booker, J., Unsworth, M., Kidd, W.S.F., Hauck, M., Alsdorf, D., Ross, A., Cogan, M., Wu, C.D., Sandvol, E., Edwards, M., 1996. Partially molten middle crust beneath southern Tibet; synthesis of Project INDEPTH results. Science 274, 1684–1688.

O'Connell, R.J., Budiansky, B., 1974. Seismic velocities in dry and saturated cracked solids. J. Geophys. Res. 79, 5412–5426.

Owens, T.J., Zandt, G., 1997. Implications of crustal property variations for models of Tibetan Plateau evolution. Nature 387, 37–43.

Owens, T.J., Zandt, G., Taylor, S.R., 1984. Seismic evidence for an ancient rift beneath the Cumberland Plateau, Tennessee; a detailed analysis of broadband teleseismic P-waveforms. J. Geophys. Res. 89, 7783–7795.

Ozacar, A.A., Zandt, G., 2004. Crustal seismic anisotropy in central Tibet: implications for deformational style and flow in the crust. Geophys. Res. Lett. 31, L23601, doi:10.1029/2004GL021096.

Rabinowicz, M., Vigneresse, J.L., 2004. Melt segregation under compaction and shear channeling: application to granitic magma segregation in a continental crust. J. Geophys. Res. 109, B04407, doi:10.1029/2002JB002372.

Roger, F., Calassou, S., Lancelot, J., Malavieille, J., Mattauer, M., Xu, Z.Q., Hao, Z.W., Hou, L.W., 1995. Miocene emplacement and deformation of the Konga Shan granite (Xianshui He fault zone, west Sichuan, China): geodynamic implications. Earth Planet. Sci. Lett. 130 (1–4), 201–216.

Rowley, D.B., 1996. Age of initiation of collision between India and Asia: a review of stratigraphic data. Earth Planet. Sci. Lett. 145, 1–13.

Roy, M., Royden, L.H., 2000a. Crustal rheology and faulting at strike-slip plate boundaries. 1. An analytic model. J. Geophys. Res. 105 (B3), 5583–5597.

Roy, M., Royden, L.H., 2000b. Crustal rheology and faulting at strike-slip plate boundaries. 2. Effects of lower crustal flow. J. Geophys. Res. 105 (B3), 5599–5613.

Royden, L.H., Burchfiel, B.C., King, R.W., Wang, E., Chen, Z.L., Shen, F., Liu, Y.P., 1997. Surface deformation and lower crustal flow in eastern Tibet. Science 276 (5313), 788–790.

Sandvol, E., Ni, J., Kind, R., Zhao, W.J., 1997. Seismic anisotropy beneath the southern Himalayas–Tibet collision zone. J. Geophys. Res. 102 (B8), 17813–17823.

Savage, M.K., 1998. Lower crust anisotropy or dipping boundaries? Effect on receiver function and a case study in New Zealand. J. Geophys. Res. 103 (B7), 15069–15087.

Silver, P.G., 1996. Seismic anisotropy beneath the continents: prosbing the depths of geology. Ann. Rev. Earth Planet. Sci. 24, 385.

Song, H.B., Lou, Z.L., 1995. The study of the basement and deep geological structures of Sichuan Basin. Earth Sci. Front. (3/4), 231–237.

Sun, J., Jin, G.W., Bai, D.H., Wang, L.F., 2003. Sounding of electrical structure of the crust and upper mantle along the eastern border of Qinghai-Tibet Plateau and its tectonic significance. Sci. China D 46, 243.

Sun, Y.S., Kuleli, S., Morgan, F.D., Rodi, W., Toksoz, M.N., 2004. Location robustness of Earthquakes in Sichuan Province, China. Seism. Res. Lett. 75 (1), 55–62.

van der Meijde, M., van der Lee, S., Giardini, D., 2003. Crustal structure beneath broad-band seismic stations in the Mediterranean region. Geophys. J. Int. 152, 729–739.

Wang, E.C., Burchfiel, B.C., 2000. Late Cenozoic to Holocene deformation in southwestern Sichuan and adjacent Yunnan, China, and its role in formfation of the southeastern part of the Tibetan Plateau. Geol. Soc. Am. Bull. 112 (3), 413–423.

Wang, C.Y., Gang, H.F., 2004. Crustal structure in Tengchong Volcano-Geothermal Area, western Yunnan, China. Tectonophysics 380, 69–87.

Wang, J.Y., Huang, S.P., 1988. Compilation of heat flow data in the China continental area. Sci. Geol. Sin. 2, 196–204.

Wang, J.H., Yin, A., Harrison, T.M., Grove, M., Zhang, Y.Q., Xie, G.H., 2001. A tectonic model for Cenozoic igneous activities in the eastern Indo-Asian collision zone. Earth Plant. Sci. Lett. 188, 123–133.

Wang, C.Y., Chan, W.W., Mooney, W.D., 2003. Three-dimentional velocity structure of crust and upper mantle in southeastern China and its tectonic implications. J. Geophys. Res. 108 (B9), 2442, doi:10.1029/2002JB001973.

Wu, Q.F., Zu, J.H., Xie, Y.Z., 1988. Basic geothermal characteristics in Yunnan Province (in Chinese). Seismol. Geol. 10 (4), 177–183.

Xu, Y.G., Menzies, M.A., Thirlwall, M.F., Xie, G.H., 2001. Exotic lithosphere mantle beneath the western Yangtze craton: petrogenetic links to Tibet using highly magnesian ultrapotassic rocks. Geology 29 (9), 863–866.

Yao, H.J., van der Hilst, R.D., de Hoop, M.V., 2006. Surface-wave array tomography in SE Tibet from ambient seismic noise and two-station analysis. I. Phase velocity maps. Geophys. J. Int. 166, 732–744.

Yao, H.J., Beghein, C., van der Hilst, R.D., submitted for publication. Surface-wave array tomography in SE Tibet from ambient seismic noise and two-station analysis: II Crustal and upper mantle structure. Geophys. J. Int.

Yuan, X.H., Ni, J., Kind, R., Mechie, J., Sandvol, E., 1997. Lithospheric and upper mantle structure of southern Tibet from a seismological passive source experiment. J. Geophys. Res. 102 (B12), 27491–27500.

Zhang, J., Langston, C.A., 1995. Dipping structure under Dourbes, Belgium, determined by receiver function modeling and inversion. Bull. Seism. Soc. Am. 85 (1), 254–268.

Zhu, L.P., Kanamori, H., 2000. Moho depth variation in southern California from teleseismic receiver functions. J. Geophys. Res. 105 (B2), 2969–2980.

Zhu, L.P., Owens, T.J., Randall, G.E., 1995. Lateral variation in crustal structure of the northern Tibetan Plateau inferred from teleseismic receiver functions. Bull. Seism. Soc. Am. 85 (6), 1531–1540.

Zorin, Yu.A., Mordvinova, V.V., Turutanov, E.Kh., Belichenko, B.G., Artemyev, A.A., Kosarev, G.L., Gao, S.S., 2002. Low seismic velocity layers in the Earth's crust beneath Eastern Siberia (Russia) and Central Mongolia: receiver function data and their possible geological implication. Tectonophysics 359, 307–327.